Journal of Advanced Ceramics
2022, **11**(12): 1873–1888
https://doi.org/10.1007/s40145-022-0653-8
ISSN 2226-4108
CN 10-1154/TQ

Research Article

Oxygen vacancy-mediated WO_3 phase junction to steering photogenerated charge separation for enhanced water splitting

Huimin LI[a,c], Qianqian SHEN[a,c,*], Han ZHANG[a,c], Jiaqi GAO[a,c], Husheng JIA[a,c,d], Xuguang LIU[a], Qi LI[e], Jinbo XUE[a,b,*]

[a]*Key Laboratory of Interface Science and Engineering in Advanced Materials of Ministry of Education, Taiyuan University of Technology, Taiyuan 030024, China*
[b]*Department of Chemistry, Tsinghua University, Beijing 100084, China*
[c]*College of Materials Science and Engineering, Taiyuan University of Technology, Taiyuan 030024, China*
[d]*Shanxi-Zheda Institute of Advanced Materials and Chemical Engineering, Taiyuan 030032, China*
[e]*School of Materials Science and Engineering, Southwest Jiaotong University, Chengdu 610031, China*

Received: June 28, 2022; Revised: August 11, 2022; Accepted: August 29, 2022

Abstract: Effective charge separation and transfer is deemed to be the contributing factor to achieve high photoelectrochemical (PEC) water splitting performance on photoelectrodes. Building a phase junction structure with controllable phase transition of WO_3 can further improve the photocatalytic performance. In this work, we realized the transition from orthorhombic to monoclinic by regulating the annealing temperatures, and constructed an orthorhombic–monoclinic WO_3 (o-WO_3/m-WO_3) phase junction. The formation of oxygen vacancies causes an imbalance of the charge distribution in the crystal structure, which changes the W–O bond length and bond angle, accelerating the phase transition. As expected, an optimum PEC activity was achieved over the o-WO_3/m-WO_3 phase junction in WO_3-450 photoelectrode, yielding the maximum O_2 evolution rate roughly 32 times higher than that of pure WO_3-250 without any sacrificial agents under visible light irradiation. The enhancement of catalytic activity is attributed to the atomically smooth interface with a highly matched lattice and robust built-in electric field around the phase junction, which leads to a less-defective and abrupt interface and provides a smooth interfacial charge separation and transfer path, leading to improved charge separation and transfer efficiency and a great enhancement in photocatalytic activity. This work strikes out on new paths in the formation of an oxygen vacancy-induced phase transition and provides new ideas for the design of catalysts.

Keywords: phase transition; tungsten oxide; lattice mismatch; density functional theory (DFT); photoelectrocatalytic water splitting

* Corresponding authors.
E-mail: Q. Shen, shenqianqian@tyut.edu.cn
J. Xue, xuejinbo@tyut.edu.cn

1 Introduction

Nowadays, the high-speed economic development of the world directly leads to the enormous pressure from both energy shortage and environmental pollution. The development and utilization of new energy have become the research hotspot of scientific community all over the world [1]. The Sun, as a huge energy reservoir, is the energy basis, on which all living things on the Earth depend [2,3]. Hydrogen energy is one of the most promising renewable energy sources because of its high energy density and eco-friendly nature. Therefore, the semiconductor photocatalysis technology that can efficiently utilize solar energy has emerged [4]. Hydrogen production through solar-driven photoelectrochemical (PEC) water splitting has become an effective solution owing to the green and pollution-free nature of the entire cycle. Hydrogen and oxygen are produced on the two sides of the photoelectrode in a PEC water splitting system, easy to be collected without additional separation and purification [5]. Since Fujishima and Honda [6] first discovered the pioneering application of n-type semiconductor TiO_2 photoanodes for water splitting under illumination in 1972, which kicked off the research on PEC water splitting for hydrogen production, conventional semiconductor photoanode materials have expanded to metal oxides, nitrides, and sulfides. However, they all faced with the challenges of serious recombination of photogenerated charges and poor visible light response [7–10].

As it is necessary to seek highly efficient, abundant, and stable photoanode materials to improve the performance of PEC water splitting, a variety of strategies have been explored to develop novel catalysts, including surface engineering [11,12], energy band structure engineering [13], and strain engineering [14,15]. Recently, nanocomposites have shown great potential for photoelectrocatalytic hydrogen evolution. Phase junction engineering is considered as an effective way to improve the photocatalytic performance in semiconductors. In most cases, there are higher requirements of structure and lattice matching for the different catalysts involved in the formation of heterostructures, and thus the preparation process is complex. Zhang *et al*. [16] achieved more efficient hydrogen production performance by constructing the anatase/rutile TiO_2 composite catalyst in 2008 and first proposed the concept of "surface-phase junctions". In their following work [17], regulable α–β polymorphic junctions were formed on the surface of Ga_2O_3, which could prominently boost the photocatalytic activity relative to α or β monophases. Considering the limited choice of compositions with appropriate compatibility and crystal structure to form the desired heterojunction interfaces, homojunctions, that is, phase junctions, are a promising route to improve water splitting performance further. Well-matched interface and robust built-in electric field between crystalline phases could accelerate electron transfer and achieve efficient separation of photogenerated charge carriers. Most of the homojunctions are formed by semiconductors with different crystalline phases in phase transition process, as reported in zinc blend/wurtzite CdSe [18], cubic/monoclinic NiP_2 [19], and black/red P [20].

Currently, WO_3 has triggered comprehensive research interest as the oxygen evolution reaction (OER) catalyst [21,22]. WO_3 is formed by sharing the vertex arrangement of octahedra consisting of one tungsten (W) atom and six oxygen (O) atoms. According to the tilt angle and rotation direction of WO_6 octahedron, WO_3 exhibits multiple crystal structures such as monoclinic, triclinic, tetragonal, orthorhombic, cubic, and hexagonal [23]. The phase transition of WO_3 occurs during annealing, cooling, and morphology evolution [24]. Meanwhile, these crystalline phases can be reversibly transformed, among which, monoclinic, orthorhombic, and hexagonal phases are stable at room temperature. The structural diversity of WO_3 provides an opportunity to construct various homojunctions [25]. It is evidenced that a built-in electric field is generated at the homogeneous interface to improve charge separation and injection efficiency [26]. Therefore, WO_3 with multiple crystalline phases and variable composition modulation is regarded as a phase junction component for the OER catalysis.

This work explored the phase–catalysis relationship by controlling the extent of orthorhombic-to-monoclinic phase transition on WO_3 to improve the efficiency of photoelectrocatalytic water splitting. The phase transition was realized during the thermal annealing process of the WO_3 prepared by a one-step hydrothermal method. The oxygen content in the annealing process was analyzed by X-ray photoelectron spectroscopy (XPS) and electron paramagnetic resonance (EPR), and the regulation of oxygen partial pressure on the formation of different crystal phases was investigated. The microscopic mechanisms of the phase junction structure and oxygen vacancy regulation on the separation and

migration of photoexcited electron–hole pairs were discussed through the density functional theory (DFT), and the catalytic performance of monoclinic–orthorhombic WO_3 towards water splitting was systematically evaluated. The results suggest that the monoclinic–orthorhombic phase junction drives the transfer kinetics of charge carriers, resulting in efficient separation. This work provides new insights into the rational design and construction of photocatalysts.

2 Experimental

2. 1 Synthesis of WO_3 nanosheets

WO_3 nanosheets were prepared on tungsten substrate by the hydrothermal method. In a typical synthesis, 1 mL of concentrated nitric acid was mixed with 15 mL of deionized water and continually stirred for at least 10 min. Then the mixture was transferred to a 25 mL Teflon-lined stainless steel autoclave. The tungsten foil with a size of 1 cm × 3 cm was sanded and mechanically polished with 400# and 600# sandpapers, and ultrasonically cleaned with acetone, ethanol, and deionized water for 30 min. The tungsten foil was placed in the autoclave and treated hydrothermally at 75 ℃ for 2 h. After the autoclave was cooled to room temperature, the tungsten substrate was taken out, rinsed with deionized water several times, and dried under vacuum at 50 ℃ for 3 h. Afterwards, the samples were placed in the center of a crucible and annealed at 250, 350, 450, and 550 ℃ for 3 h with a heating rate of 3 ℃·min^{-1} in an air atmosphere. The WO_3 materials annealed at 250, 350, 450, and 550 ℃ are recorded as WO_3-250, -350, -450, and -550, respectively. The macroscopic profiles are shown in Fig. S1 in the Electronic Supplementary Material (ESM).

2. 2 Characterization

The crystal structures of the as-obtained samples were characterized on an X-ray diffractometer (D/MAX-2400, Rigaku, Japan) with Cu Kα radiation (λ = 1.5406 Å) at 40 kV and 40 mA for physical phase analysis. The field emission scanning electron microscopy (FESEM; JSM-6700F, JEOL, Japan) and energy dispersive X-ray spectroscopy (EDS) were used to observe the surface morphologies and chemical compositions of the as-obtained samples. The high-resolution transmission electron microscopy (HRTEM) images were taken on a microscope (JEM-2100F, JEOL, Japan) at an accelerating voltage of 200 kV. The surface compositions and valence states of elements were measured by the X-ray photoelectron spectrometer (ESCALAB 250Xi, Thermo Fisher, USA) with a monochromatic Al Kα radiation X-ray source. The binding energy was calibrated by the C 1s peak (284.8 eV) as the reference. The EPR spectrometry was performed by using an EPR equipment (EMX, Bruker, Germany). The Raman spectrum excited at 532 nm was recorded on a confocal micro-Raman spectrometer (XploRa, HORIBA Scientific, Japan) with a spectral resolution of 2 cm^{-1}. The optical absorption properties of the samples were tested on an ultraviolet–visible (UV–Vis) spectrophotometer (U-3900, Hitachi, Japan) equipped with an integrating sphere attachment using $BaSO_4$ as the reference. The surface photovoltage (SPV) system consists of a 500 W Xe lamp (CHF-XM500W, Perfect Light, China), a monochromator (Omni-λ300, Zolix, China), a lock-in amplifier (SR830, Stanford Research Systems, USA) with a light chopper (SR540, Stanford Research Systems, USA), a photovoltaic cell, and a computer. Both the monochromator and the lock-in amplifer are controlled by the computer.

2. 3 PEC experiment

All PEC measurements were performed in a standard three-electrode system in an electrochemical workstation (CHI660E, CH Instruments, China), using Pt sheet (1 cm × 3 cm) as the counter electrode, saturated calomel electrode (SCE) as the reference electrode, and the as-obtained samples as the working electrode. The effective mass of WO_3 film is estimated to be 10 mg (Fig. S2 in the ESM). The tests were carried out in 0.5 M Na_2SO_4 aqueous solution at room temperature. A 300 W Xe lamp with an irradiation of 100 mW·cm^{-2} was equipped with a 420 nm cutoff filter to simulate AM 1.5 G. The transient photocurrent was recorded at a bias voltage of 0.6 V vs. SCE with an interval of 20 s. The electrochemical impedance spectroscopy (EIS) measurements were performed at 0.6 V bias voltage vs. SCE with the frequency range of 10^{-2}–10^5 Hz. The Mott–Schottky (M–S) curves were measured at 10 mV/s and 1000 Hz.

2. 4 Photoelectrocatalytic performance evaluation

Photoelectrocatalytic water splitting experiments were conducted in a closed quartz reaction cell with the electrolyte containing 0.5 M Na_2SO_4 solution in a

three-electrode system with Pt sheet, SCE, and the as-obtained samples as the counter, reference, and working electrodes, respectively. The whole reaction process was kept under magnetic stirring. Before the test, the reaction cell was purged with nitrogen gas for 30 min to remove the impurity gas inside. Then, the photocatalytic test was performed with a 300 W Xe lamp with a 420 nm cut-off filter. Gas production was detected by a gas chromatography (GC9790 II, Zhejiang Fuli Co., Ltd., China) equipped with a thermal conductivity detector (TCD).

2. 5 Theoretical calculations

First-principles calculations were performed with the material simulation software of Cambridge Sequential Total Energy Package (CASTEP) based on the DFT. The ground states of m-WO_3 and o-WO_3 were established by theoretical calculations and the X-ray diffraction (XRD) refinement. The ultra-soft pseudopotential (USPP) was used to describe the interaction between electrons and ions, and the exchange-correlation potential between electrons was calculated by using the Perdew–Burke–Ernzerhof (PBE) density function in the generalized gradient approximation. The plane wave cutoff energy was set to 300 eV, and the Brillouin zone was sampled with 2 × 2 × 2 Monkhorst–Pack grids for geometry optimization and energy band structure calculation. To build the m-WO_3/o-WO_3 interface, two layers of o-WO_3 (100) were placed on top of a three-layer m-WO_3 (001) slab. In the structure optimization, the maximum force per atom was converged to 0.01 eV·Å^{-1}, and the convergence threshold for energy was set at 5.0×10^{-6} eV·atom^{-1}.

3 Results and discussion

The samples are synthesized through a simple two-step process, as shown in Fig. 1. The microscopic morphologies of the as-prepared materials under different annealing temperatures are observed by using the FESEM, as shown in Fig. S3 in the ESM. The structures of annealed WO_3 samples are nanosheets perpendicular to the W substrate and closely adhered to the W substrate. The WO_3 nanosheets gradually increase in thickness and distort to some extent as the annealing temperature rises from 250 to 550 ℃. It is reported that the formation of WO_3 follows a dissolution–recrystallization mechanism under hydrothermal conditions [27]. The strongly oxidizing nitric acid initially oxidizes the tungsten foil to WO_4^{2-}, while the insoluble $WO_3\cdot H_2O$ is deposited on the surface of the tungsten substrate. The as-formed pale yellow $WO_3\cdot nH_2O$ hydrate is converted into WO_3 phase with removal of water molecules during subsequent annealing, accompanied with color changes [28]. The formation mechanism can be described as Reactions (1) and (2):

$$2WO_4^{2-} + 4H^+ \rightarrow 2H_2WO_4 \rightarrow 2WO_3\cdot H_2O \quad (1)$$

$$WO_3\cdot nH_2O \rightarrow WO_{3-x} + nH_2O + xV_o + 2xe^- \quad (2)$$

where V_o represents the oxygen vacancy.

The color changes from pale yellow to dark blue during annealing at 450 ℃, indicating the presence of non-stoichiometric WO_3, which is due to the transfer of electrons in WO_3 allowing partial reduction from W^{6+} to W^{5+}, resulting in the formation of oxygen vacancy defects. The EDS elemental mappings display the uniform distributions of tungsten and oxygen elements in the WO_3 nanosheets.

Furthermore, WO_3 phase junctions with different monoclinic/orthorhombic phase ratios were fabricated by tuning the annealing temperatures to verify the feasibility of phase transition. The crystal structures of orthorhombic WO_3 (o-WO_3) and monoclinic WO_3 (m-WO_3) are shown in Fig. S4 in the ESM. As shown in Fig. 2(a), it is obvious that there is only a diffraction

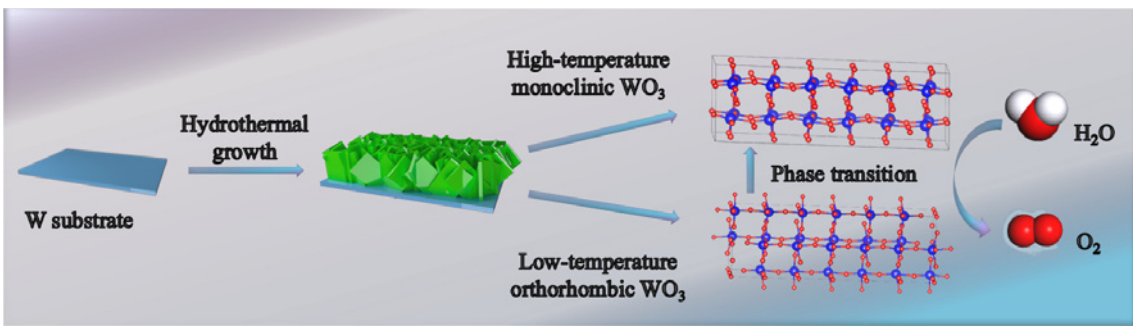

Fig. 1 Diagram of the preparation for WO_3 samples. Blue balls are W atoms, and red balls are O atoms.

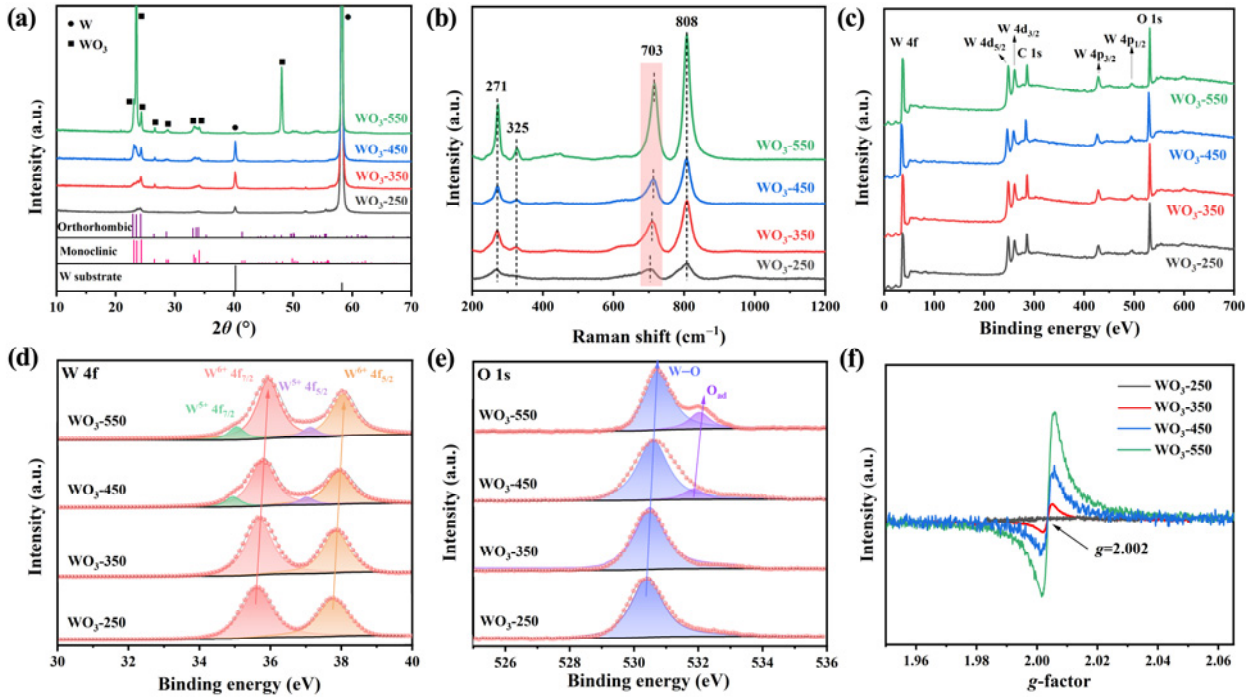

Fig. 2 (a) XRD patterns of different WO_3 photoelectrodes. (b) Raman spectra of all samples. (c) Survey XPS spectra. High-resolution XPS spectra of (d) W 4f and (e) O 1s. (f) EPR of all samples. Note: O_{ad} is the adsorbed oxygen.

peak of o-WO_3 at 250 ℃, while WO_3-350, -450, and -550 show both the characteristic peaks of o-WO_3 and m-WO_3. A minor diffraction peak with preferred orientation of tungsten appears because of the rolled tungsten substrate. A series of diffraction peaks in the XRD pattern of WO_3-250 match well with the orthorhombic structure (PDF #71-0131) assigned to the space group of *Pmnb*. The diffraction peak at 24.3° of the WO_3-350 sample belongs to the orthorhombic phase, while the two diffraction peaks at 23.1° and 23.5° corresponding to the (002) and (020) planes, respectively, are detected as typical features for the monoclinic structure (PDF #72-0677) with a space group of $P2_1/n$. It is generally acknowledged that the intensity of the diffraction peak in the XRD patterns is related to the crystallinity. With the increase of annealing temperature, the samples show higher peak intensity. The enlarged view of the XRD patterns in the range of 22.5°–25° in Fig. S5 in the ESM indicates that the phase transition takes place at 350 ℃. As the annealing temperature rises from 250 to 550 ℃, the intensities of characteristic peaks for m-WO_3 located at 23.1°, 23.5°, and 28.7° gradually increase, which demonstrate a temperature-dependent phase transition of WO_3 in the annealing process. To determine the exact ratio of o-WO_3 to m-WO_3 as a function of temperature, a Rietveld refinement of the XRD data was performed by using General Structure Analysis System (GSAS) software [29]. The specific weight percentages of o-WO_3 and m-WO_3 in the samples are obtained in Fig. S6 in the ESM. The results of the profile coinciding factors (R_{wp} and R_p) and the contents of orthorhombic and monoclinic phases are displayed in Table S1 in the ESM. The R_{wp} values of all WO_3 samples are less than 15%, indicating the reliability of the refinement results.

The Raman spectroscopy was utilized to identify and investigate the difference of chemical bonds for WO_3. Four obvious Raman characteristic peaks of 703, 808, 271, and 325 cm^{-1} can be observed in Fig. 2(b). The peaks located at 271 and 325 cm^{-1} could be assigned to the bridging oxygen bending vibration of the W–O–W [30,31]. The characteristic peaks centered at 703 and 808 cm^{-1} corresponded to the stretching vibration of the W–O–W bond in the [WO_6] octahedron [32]. The diffraction peak located at 703 cm^{-1} shows a red shift with increasing the temperature. This result indicates the significant change in the original coordination environment, where the corresponding changes in W–O–W bond length and polyhedral deformation are closely related to the structural transformation and partial loss of oxygen atoms in the WO_3 lattice. To

reveal the contributions of the surface chemical environment and interaction of o-WO_3 and m-WO_3 phases, the XPS technique was used to characterize the bonding properties of the surface W–O of all WO_3 samples. As seen from the survey XPS spectra in Fig. 2(c), tungsten and oxygen elements exist in all WO_3 samples with no other impurities. The high-resolution spectra of W 4f are deconvoluted into two pairs of peaks by Gaussian fitting, corresponding to the typical binding energies of two different W oxidation states (Fig. 2(d)). The binding energies of W 4f at 35.6 and 37.7 eV in WO_3-250 can be attributed to the photoelectrons generated from the spin–orbit splitting of the $4f_{7/2}$ and $4f_{5/2}$ of W^{6+} species, respectively [33,34]; while for WO_3-450 and WO_3-550, the W^{6+} $4f_{7/2}$ and W^{6+} $4f_{5/2}$ peaks are positively shifted, and the weak peaks at 35.2 and 37.3 eV belong to W^{5+} species, indicating that W^{6+} oxidation state is dominant at the WO_3 surface. The formation of low valence states is usually accompanied by the emergence of oxygen vacancies [35]. To explore the generation of oxygen vacancies from the O 1s spectra, the O 1s peak is deconvoluted into two peaks (Fig. 2(e)). The peak of lattice oxygen at 530.2 eV in WO_3-250 is attributed to W^{6+}–O, while those at 531.8 and 532 eV are characteristic of adsorbed oxygen associated with surface oxygen vacancies, suggesting the presence of a small number of localized electrons in the WO_3-450 and WO_3-550 nanosheets [36]. With the increase of m-WO_3 contents, the slight positive shifts of the W 4f and O 1s peaks with respect to WO_3-250 are caused by the electron transfer from o-WO_3 to m-WO_3 and the electron coupling between the two phases near the interface [37], resulting in o-WO_3 losing electrons while m-WO_3 getting electrons, thus creating an internal electric field at the phase interface. In addition, the EPR spectroscopy was performed to further verify the oxygen vacancies in WO_3 photoelectrodes. Clearly, the peak ESR signal at *g*-tensor of 2.002 corresponds to the single electron capture oxygen vacancy [19]. As the temperature increases, it shows a stronger EPR signal intensity, as shown in Fig. 2(f). Since the oxygen vacancy concentration is proportional to the intensity of the EPR signal peak, this demonstrates that WO_3-550 has the highest oxygen vacancy concentration.

On the basis of the refinement results, it can be assumed that high annealing temperatures could be beneficial to the increase of m-WO_3 content. Meanwhile, the lattice parameters of o-WO_3 are found to change at different annealing temperatures during the phase transition from orthorhombic WO_3 to monoclinic WO_3, which can be described by the changes in the octahedral tilt system or the displacement of tungsten away from octahedral center. Specifically, the lattice constants α and γ are the same for o-WO_3 and m-WO_3, and there is a slight difference in β (o-WO_3: $\beta = 90°$; m-WO_3: $\beta = 90.881°$). Therefore, the following coordinate system is established to investigate the variation of β in W–O octahedra at different annealing temperatures. The crystal structures of o-WO_3 and m-WO_3 are shown in Figs. 3(a) and 3(b), respectively, and the changes of bond lengths and bond angles in o-WO_3 and m-WO_3 during annealing are listed in Table 1. The W–O bond lengths and O–W–O bond angles change with the temperature increasing, and then the W–O octahedral structure deforms (distortion, tilt, etc.). In o-WO_3, the bond angle of O_1–W–O_2 gradually becomes larger, and the W–O_1, W–O_2, and W–O_3 bond lengths gradually shorten with the increase of temperature, indicating that the tungsten atoms located at the center of the octahedral structure move towards the octahedral prism, and the *c*-component of the tungsten displacement is significantly greater than that in the *a*–*b* plane, while the W–O bond length stretches in the other direction, leading to the phase transition in WO_3 catalysts. The displacement change of W causes the octahedral distortion, and manifests as the phase transition from orthorhombic to monoclinic when the distortion energy

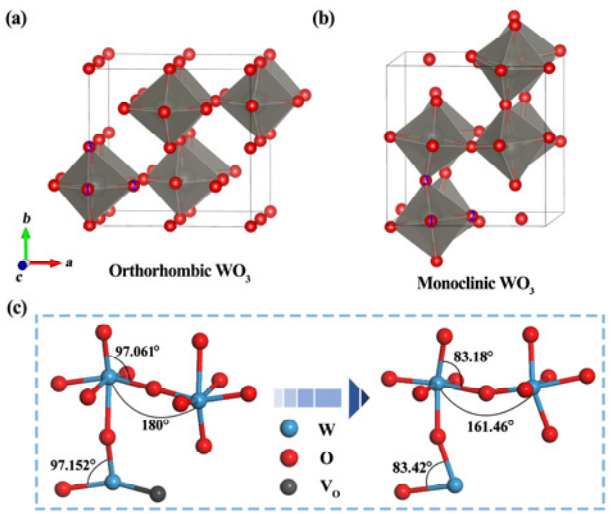

Fig. 3 Crystal structure models of (a) orthorhombic and (b) monoclinic phases. Grey ball are the W atoms, and red balls are O atoms. Among these, 1, 2, and 3 are the different positions of oxygen atoms. (c) Oxygen vacancy-induced transition mechanism from orthorhombic to monoclinic.

Table 1 Bond lengths and bond angles of four samples

		WO_3-250	WO_3-350		WO_3-450		WO_3-550	
		o-WO_3	o-WO_3	m-WO_3	o-WO_3	m-WO_3	o-WO_3	m-WO_3
W–O distance (Å)	W–O_1	1.979	1.970	1.707	1.962	1.658	1.957	1.623
	W–O_2	1.816	1.815	1.937	1.814	1.914	1.812	1.890
	W–O_3	1.868	1.864	1.737	1.855	1.721	1.848	1.714
O_1–W–O_2 bond angle (°)		92.09	92.09	96.75	92.12	97.33	92.50	98.66

of the system accumulates to a certain degree. The stoichiometry of WO_3 samples is further evaluated by calculating the ratio of lattice oxygen to all tungsten atoms (W^{5+}+W^{6+}) in the WO_3 photoelectrodes (Table S2 in the ESM). The results show that the surface atomic O/W ratio is significantly lower than the stoichiometric ratio, and WO_3-550 has the smallest atomic O/W ratio. Therefore, the WO_3 photoelectrode surface undergoes "hypoxia" through the following process:

$$2W^{6+}+O^{2-}\rightarrow 2W^{5+}+\frac{1}{2}O_2+V_o$$

where O^{2-} is the lattice oxygen. This demonstrates that W^{5+} is induced by oxygen vacancies during the experiment. Furthermore, the absence of oxygen changes the bond lengths and bond angles of W–O octahedra, prompting the distortion of the W–O octahedron structure towards a low-energy stable state (Fig. S7 in the ESM), transforming from an orthorhombic phase with high spatial symmetry to a monoclinic phase with low spatial symmetry, which indicates that the formation of oxygen vacancies regulates the phase transition from o-WO_3 to m-WO_3 (Fig. 3(c)).

The microstructures and morphologies of WO_3-450 and WO_3-550 are shown in Fig. 4, and WO_3-450 exhibits a uniform nanosheet-like morphology with a rectangular structure with a thickness of about 50 nm (Fig. 4(a)). The HRTEM images further provide direct evidence for the formation of heterojunction. The distinct interplanar distances are observed with the *d*-spacings of 0.265 and 0.385 nm, assigned to the (202) facet of o-WO_3 and the (002) facet of m-WO_3, respectively (Fig. 4(b)). The coexistence of monoclinic and orthorhombic WO_3 is further confirmed by the fast Fourier transformation (FFT) results of the corresponding region (Fig. 4(c)), which directly demonstrate that o-WO_3 and m-WO_3 are interwoven at the interface to form well-contact phase junction structures in the WO_3-450 sample. To better understand the interface structure of o-WO_3/m-WO_3 phase junction, the lattice mismatch (*m*) of o-WO_3/m-WO_3 is estimated by considering the angular mismatch using Eq. (3) [38–41]:

$$m=\frac{|d_1/\sin\theta_1-d_2/\sin\theta_2|}{d_1/\sin\theta_1} \quad (3)$$

where d_1 and d_2 correspond to the interplanar distances of m-WO_3 (002) and o-WO_3 (002), respectively; and θ_1 and θ_2 are the angles of m-WO_3 (002) and o-WO_3 (002) against the phase interface measured at 23° and 23°, respectively.

Figure 4(d) is a schematic presenting the interfacial lattice relations of m-WO_3 (002) and o-WO_3 (002). The interfacial lattice mismatch between m-WO_3 (002) and o-WO_3 (002) in the WO_3-450 nanosheets reaches 0.7%. The o-WO_3/m-WO_3 phase junction structure of the WO_3-550 sample is shown in Figs. 4(e)–4(h), with

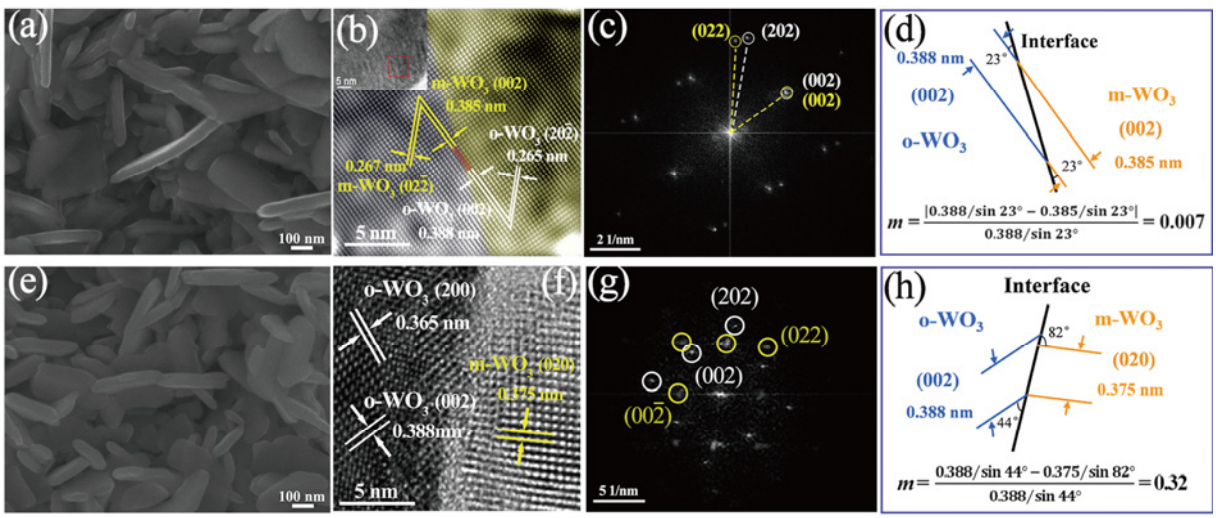

Fig. 4 Morphologies and microstructures of the as-prepared samples: (a, e) SEM images, (b, f) HRTEM images, (c, g) FFT patterns of (b) and (f), respectively; and schematics of the o-WO_3/m-WO_3 phase interface for (d) WO_3-450 and (h) WO_3-550.

an interfacial lattice mismatch of 32% between m-WO_3 (020) and o-WO_3 (002). The significant difference in lattice mismatch between o-WO_3 and m-WO_3 is considered to be an important factor in determining the photoelectrocatalytic performance. The small lattice mismatch at the interface causes minimal lattice distortion energy, reduces the nucleation energy barrier, and promotes the formation of phase junctions. Importantly, the lattice connection between m-WO_3 (002) and o-WO_3 (002) in WO_3-450 results in fewer defects and abrupt interfaces. This bonding at the phase interface is achieved by covalent bonding at atomic level rather than van der Waals forces, which allows for maximum separation and transfer of photogenerated carriers [20]. The microstructure and morphology of the WO_3-250 sample are shown in Fig. S8 in the ESM. Moreover, given the degree of phase transition, the phase junction density is believed to differ in each WO_3 sample, and the o-WO_3/m-WO_3 phase junction density is in an equilibrium state.

The photoelectrocatalytic performance of WO_3 was evaluated in Na_2SO_4 solution without using any sacrificial agents at a bias potential of 1.23 V (vs. reversible hydrogen electrode (RHE)) under visible light illumination. The ability of the photoelectrodes for overall water splitting into H_2 and O_2 was also investigated. The hydrogen and oxygen production of all WO_3 samples increase approximately linearly, as shown in Fig. 5(a). In Fig. 5(b), WO_3-250 as a pure orthorhombic phase exhibits poor oxygen production rate, and WO_3-450 exhibits the highest oxygen production rate of 7.93 $\mu mol \cdot cm^{-2} \cdot h^{-1}$, which is around 36, 2.8, and 1.2 times that of WO_3-250, -350, and -550, respectively, indicating that the o-WO_3/m-WO_3 phase junction greatly improves the performance of water splitting. This result provides the conclusive evidence that this excellent activity can be attributed to the highly matched lattice between o-WO_3 and m-WO_3 in the phase junction, which significantly boosts the photoelectrocatalytic performance by improving the interfacial charge separation. The atomic-level smooth interfacial region between o-WO_3 and m-WO_3, which facilitates charge separation and transfer, must play a key role in its excellent photocatalytic performance. As shown in Fig. 5(c), WO_3-450 shows no significant decrease in activity after five cycles, manifesting its reproducibility and stability in the catalytic process. The oxygen production rates of various catalysts reported in the literature are compared in Fig. 5(d) and Table S3 in the ESM. To further confirm the long-term

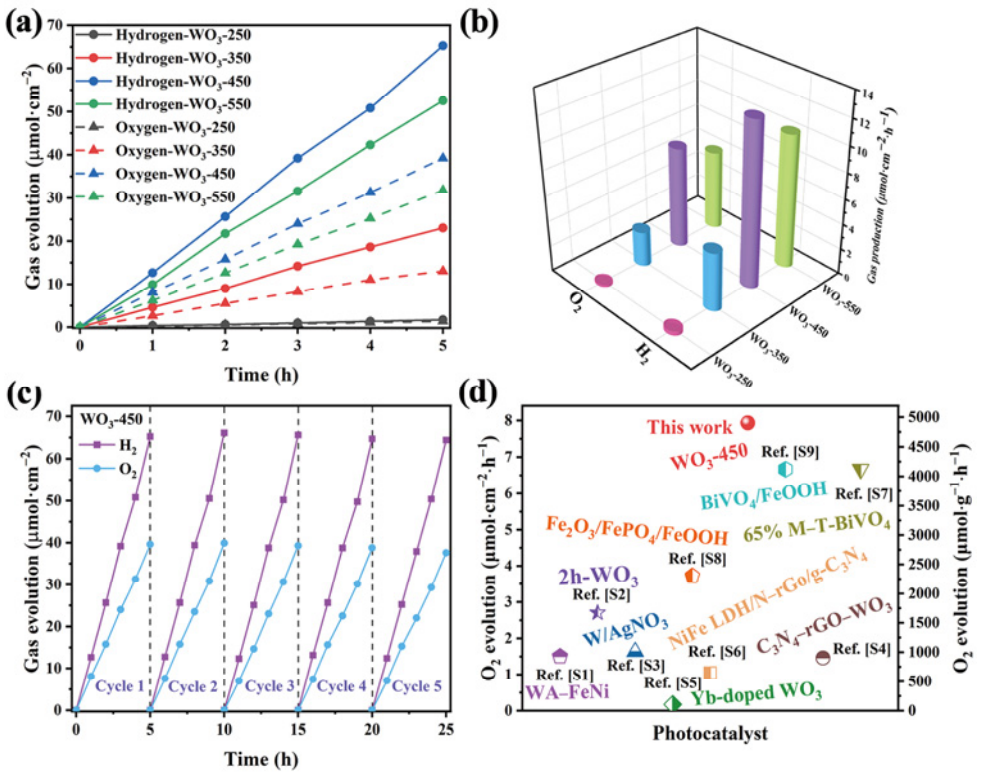

Fig. 5 (a) Photoelectrocatalytic overall water splitting and (b) rates of H_2 and O_2 production over various samples, (c) photoelectrocatalytic durability test, and (d) oxygen evolution rates for WO_3-450 in comparison with other photocatalysts.

stability of o-WO_3/m-WO_3 phase junction, the surface morphology and chemical structure were checked after 5-h oxygen production. The SEM and XRD analyses reveal that WO_3-450 maintains its original morphology and crystal structure after 5-h test, with no significant changes with respect to those before test, demonstrating its high stability in catalytic activity and structure (Fig. S9 in the ESM).

To verify the effect of phase junction on OER in WO_3 photoanodes, a series of PEC tests were performed at a bias potential of 1.23 V (vs. RHE) under visible light irradiation. First, the linear sweep voltammetry (LSV) measurement was carried in a 0.5 M Na_2SO_4 electrolyte for WO_3 photoelectrodes. As shown in Fig. 6(a), all samples show negligible currents under dark conditions, and the WO_3-250 electrode exhibits a relatively low photocurrent density. A significant increase in photocurrent density is observed in the WO_3-450 electrode, which gives the highest photocurrent density (0.31 mA·cm^{-2} at 1.23 V vs. RHE), 36 times higher than WO_3-250. This is attributed to the phase junction structure formed during the phase transition from o-WO_3 to m-WO_3. The transient photocurrent response indicates that WO_3-450 exhibits the highest photocurrent density of 0.26 mA among all samples, confirming its best charge transfer and separation efficiency (Fig. 6(b)). Notably, the construction of o-WO_3/m-WO_3 phase junction not only facilitates photon absorption but also enhances the separation of photogenerated charge–hole pairs. To gain insight into the charge transport behavior inside the electrode, the EIS (Fig. 6(c)) is adopted to evaluate the charge transfer kinetics at the interface. The charge transfer resistance (R_{ct}) at the semiconductor–electrolyte interface is assessed from the arc radius of the Nyquist plots. Obviously, there is only a semi-circular arc in the EIS Nyquist plots of the four photoanodes, indicating that the transport of most carrier electrons is the primary rate-controlling step between frequency ranges of 10^{-2}–10^5 Hz. The fitted results of equivalent circuit (Table S4 in the ESM) show that the R_{ct} is 19,944, 1087, 53.46, and 893 Ω for WO_3-250, -350, -450, and -550, respectively, which demonstrates that WO_3-450 has the lowest R_{ct} and consequently the highest conductivity for the accelerated transfer and transmission of photo-generated charges, and also for a good charge separation in WO_3-450. Thus the positive role of phase junctions in the catalytic process is proved. Next, the cyclic voltammetry (CV) measurements are performed on all samples to evaluate the double-layer capacitance (C_{dl}) of the WO_3 photoelectrodes (Fig. S10 in the ESM), and roughly estimate the electrochemical active surface area (ECSA) based on the C_{dl} of the normalized electrode. The C_{dl} values obtained from the slopes for the corresponding samples in Fig. 6(d) are 9.2, 1.6, 0.7, and 0.2 mF·cm^{-2} for WO_3-450, -550, -350,

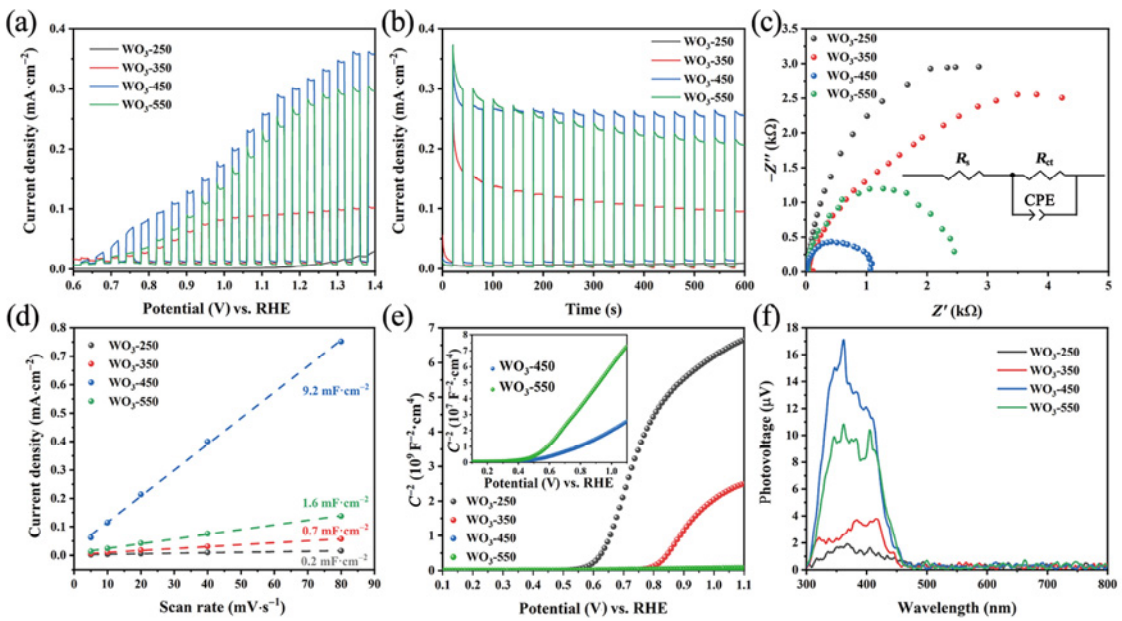

Fig. 6 (a) LSV curves of different WO_3 samples (scan rate = 1 mV·s^{-1}), (b) transient photocurrent responses, (c) EIS Nyquist plots (the inset is the equivalent circuit model for fitting the EIS data), (d) C_{dl} for various catalysts, (e) M–S plots, and (f) SPV spectra for various WO_3 samples.

and -250, respectively, which indicates that WO_3-450 exposes more active sites compared with the other samples, promoting the surface reaction and greatly enhancing its catalytic performance. The carrier concentration and flat band potential on the photoanode surface can be estimated from the M–S plots. The carrier concentration can be estimated by Eqs. (4) and (5) [42]:

$$\frac{1}{C^2}=\left(\frac{2}{e\varepsilon\varepsilon_0}\right)\left(E-E_{\mathrm{fb}}-\frac{kT}{e}\right) \tag{4}$$

$$N_{\mathrm{d}}=\frac{2}{e\varepsilon\varepsilon_0}\left[\frac{\mathrm{d}\left(1/C^2\right)}{\mathrm{d}E}\right]^{-1} \tag{5}$$

where C is the capacitance at the semiconductor/electrolyte interface, e (1.602×10^{-19} C) is the electronic charge, ε_0 (8.834×10^{-12} F·m^{-1}) is the vacuum permittivity, ε (300) is the dielectric constant of WO_3, E is the applied voltage, E_{fb} is the flat band potential, k is the Boltzmann constant, T is the absolute temperature, and N_{d} is the charge carrier concentration.

As shown in Fig. 6(e), the positive slopes for all WO_3 samples exhibit the nature of n-type semiconductors, in which electrons are the dominant charge carriers. Importantly, WO_3-350, -450, and -550 show smaller slopes than WO_3-250, which means that the construction of phase junctions can significantly increase the concentration of carriers. WO_3-450 shows the highest N_{d} value, about 600 times that of WO_3-250, which is in very good agreement with the EIS results, suggesting that more holes can migrate to the surface to participate in the redox reaction of water, thus enhancing the PEC performance. The SPV spectrometry is used to analyze the transfer pathway of carriers in the WO_3 photoanodes. The signal of SPV is attributed to the change in surface potential barrier before and after illumination, and the signal intensity increases with the separation and transfer efficiency of photogenerated charges. The positive photovoltage signal illustrates that all samples have the characteristics of n-type semiconductors (Fig. 6(f)). WO_3-250 exhibits a weak SPV response in 300–460 nm, while other WO_3 samples with phase transition show much stronger SPV intensity. This clearly suggests that the construction of phase junction improves the separation and transfer of photogenerated charges in WO_3. It is generally believed that the migration of holes to the catalyst surface is accompanied by a decreasing phase angle towards 0°. WO_3-450 exhibits the strongest SPV intensity with more negative phase angles (Fig. S11 in the ESM). This indicates that the separation and transfer of charge carriers are greatly promoted by o-WO_3/m-WO_3 phase junction structure, which contributes to the enhanced photocatalytic performance.

The UV–Vis diffuse reflectance spectroscopy is used to evaluate the light absorption properties of the catalysts. As shown in Fig. 7(a), all samples exhibit strong absorption in the UV region. The absorption band edge of WO_3-250 and WO_3-350 appears at about 500 and 550 nm, respectively, with a weak band-tail absorption region derived from the effects of lattice defects [43]. Whereas WO_3-450 and WO_3-550 show a wide range of absorption from the UV to near-infrared regions, where the light absorption intensity even reaches the intrinsic absorption of the samples. This is because the presence of oxygen vacancies leads to the formation of defect energy levels, narrowing the WO_3 band gap and broadening the light absorption range [44]. Figure 7(b) shows the WO_3 band gap determined by the Kubelka–Munk equation and the Tauc plot equation. WO_3-250 is of pure orthorhombic phase with a band gap value estimated to be about 2.50 eV [45,46]. Its flat band potential (E_{fb}) is determined to be 0.63 V (vs. RHE) (Fig. 7(c)) by extrapolating the linear region of the M–S plot. For n-type semiconductors, it is generally assumed that E_{fb} is about 0.2 eV more positive than the conduction potential (E_{CB}) [46], and thus the E_{CB} of WO_3-250 can be discerned to be 0.43 V (vs. RHE). The valence band (VB) of WO_3-250 is obtained as 2.93 eV by extrapolating the linear part to the baseline of the XPS VB spectrum in Fig. 7(d), which is consistent with the estimated band gap value [47]. It shows that the band gap value of monoclinic phase WO_3 is approximately 2.30 eV [48]. With the gradual transition from o-WO_3 to m-WO_3, the band gap of WO_3 photoelectrodes decreases, with that of WO_3-450 being the minimal. This is because the introduction of oxygen vacancies narrows the band gap and greatly improves the utilization of visible light in WO_3-450.

To elucidate the interfacial interaction between o-WO_3 and m-WO_3 in the o-WO_3/m-WO_3 junction at the atomic level, the DFT calculations were performed with o-WO_3, m-WO_3, and o-WO_3/m-WO_3 junction as models. The band structures and density of states (DOS) of both o-WO_3 and m-WO_3 models are calculated on the basis of the XRD refinement. The results are presented in Figs. 8(a) and 8(b). According

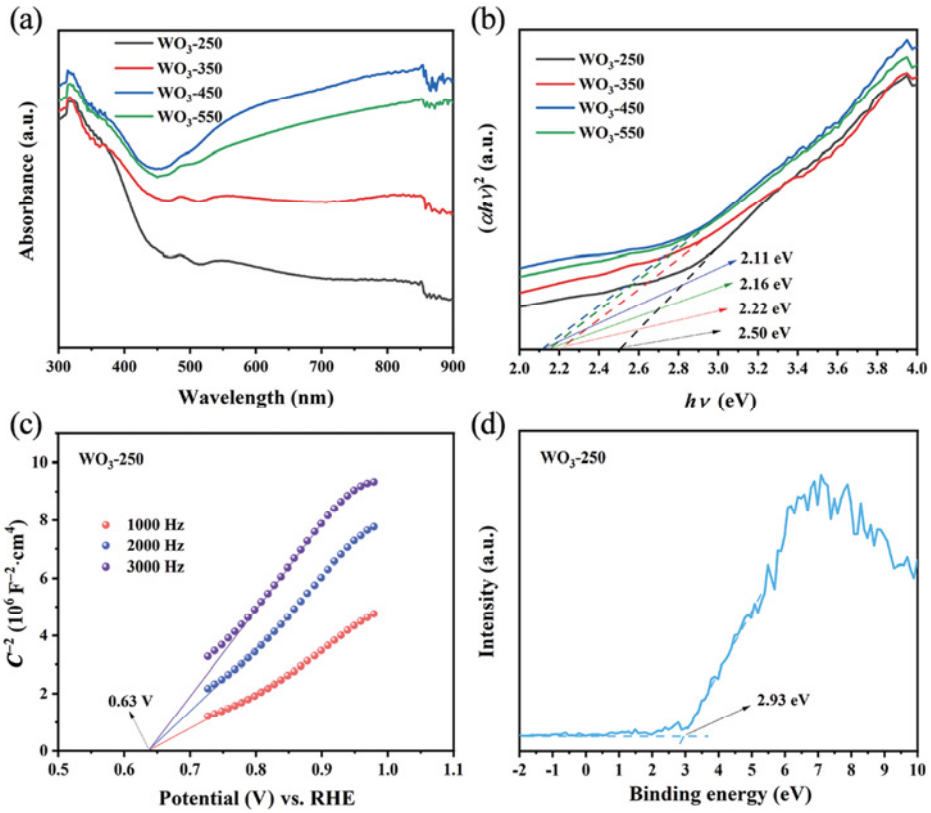

Fig. 7 (a) UV–Vis absorption spectra and (b) corresponding optical band gaps (where α in the *Y*-axis title represents the absorbance, h represents the Planck constant, and υ represents the frequency); (c) M–S plot and (d) VB spectrum of WO_3-250.

to the energy band diagram, o-WO_3 has a direct band gap of about 1.94 eV, close to the experimental optical band gap (2.5 eV) with a significant underestimation [49]. Similarly, m-WO_3 shows a direct band gap of 1.76 eV. From the DOS results, it can be seen that the VB of WO_3 is mainly occupied by W 5d and O 2p orbitals in the range from −7 to 0 eV. Above the Fermi energy level (E_F), the conduction band (CB) of o-WO_3 consists of W 5d and O 2p orbitals, while that of m-WO_3 is dominated by W 5d orbital. The redox capacity of the semiconductor is assessed by VB and CB positions. The E_{CB} and VB edge potentials (E_{VB}) of the two semiconductors at the zero charge point are roughly calculated according to Eqs. (6) and (7) [50,51]:

$$E_{CB} = \chi - E_e - 0.5E_g \quad (6)$$

$$E_{VB} = E_{CB} + E_g \quad (7)$$

where χ is the absolute electronegativity of the semiconductor, which is 6.53 eV for WO_3; E_e (4.5 eV) is the energy of free electron at hydrogen scale; and E_g is the band gap of the semiconductor. The band gaps calculated for o-WO_3 and m-WO_3 are 1.94 and 1.76 eV, respectively. Thus, the band edge positions of CB and VB of o-WO_3 are 1.06 and 3.00 eV, respectively. Similarly, the potentials of CB and VB of m-WO_3 are 1.15 and 2.91 eV, respectively.

In a phase junction system, the Fermi level of semiconductor affects the charge transfer path. Accordingly, the work functions (Φ) of o-WO_3 and m-WO_3 were calculated by using the first-principles DFT [52,53]. In Figs. 8(c) and 8(d), the electrostatic potentials on the surfaces of o-WO_3 (100) and m-WO_3 (001) are displayed. It is clear that the work functions of o-WO_3 and m-WO_3 are 5.62 and 5.53 eV, respectively. The calculation results of the work functions are related to the construction of the calculation model and the selection of some corresponding parameters (such as cut-off energy). When the two phases are in contact, since o-WO_3 has a higher work function and a lower Fermi level than m-WO_3, electrons migrate from m-WO_3 to o-WO_3 until the Fermi level reaches equilibrium. At this point, o-WO_3 is negatively charged, while m-WO_3 is positively charged at the interface. The energy band of o-WO_3 bends downward, while that of m-WO_3 upward. Therefore, a built-in electric

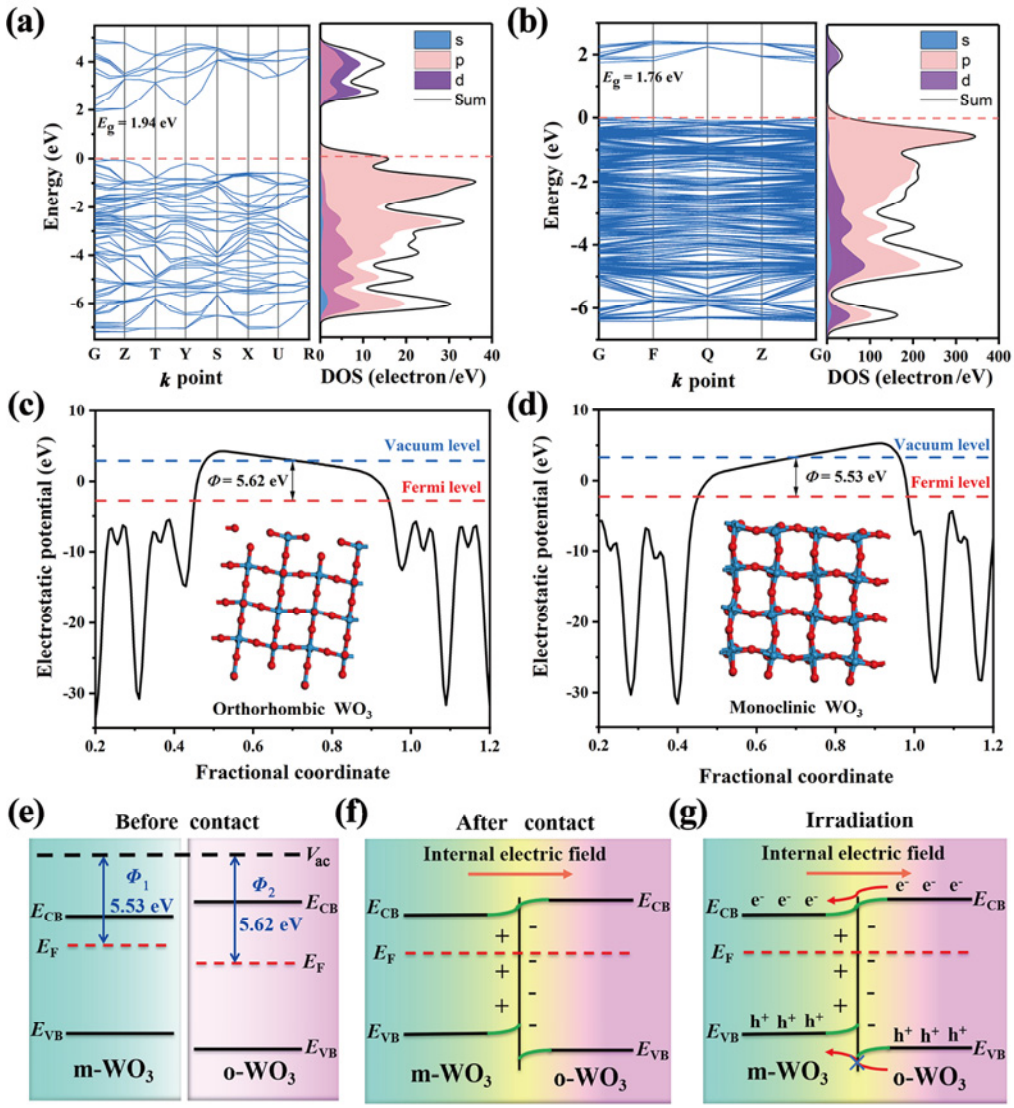

Fig. 8 Calculated band structures and work functions of (a, c) o-WO_3 and (b, d) m-WO_3; (e–g) schematic diagrams of the formation process of the o-WO_3/m-WO_3 electron transfer mechanism.

field is formed, and a band edge bending occurs [54–56]. After excitation by incident light, the o-WO_3/m-WO_3 phase junction has a staggered arrangement of energy band structure at the interface, the photogenerated electrons from o-WO_3 are injected into the CB of m-WO_3, while the photogenerated holes on the VB of o-WO_3 are not transferred to m-WO_3, owing to the existence of electric field repulsion and energy band barrier. The formation mechanism of o-WO_3/m-WO_3 phase junction is shown in Figs. 8(e)–8(g). The presence of internal electric field facilitates the separation of photogenerated electron–hole pairs, which in turn improves the photocatalytic activity of WO_3 [57]. To reveal the charge transfer path at the o-WO_3/m-WO_3 junction interface, the charge difference density of the o-WO_3/m-WO_3 junction is calculated. The charge redistribution occurs mainly at the interface between o-WO_3 and m-WO_3. As shown in Fig. S12 in the ESM, where the red and blue regions represent the charge accumulation and depletion, respectively, o-WO_3 surface is mainly blue, while m-WO_3 surface is mainly red, indicating a flow of electron from o-WO_3 to m-WO_3, which leads to the built-in electric field in the o-WO_3/m-WO_3 phase junction structure.

On the basis of the experimental results and DFT calculations, it is strongly demonstrated that the o-WO_3/m-WO_3 phase junction significantly improves the photocatalytic activity, with the enhancement mechanism shown in Fig. 9. The o-WO_3/m-WO_3 phase junctions are constructed during the phase transition

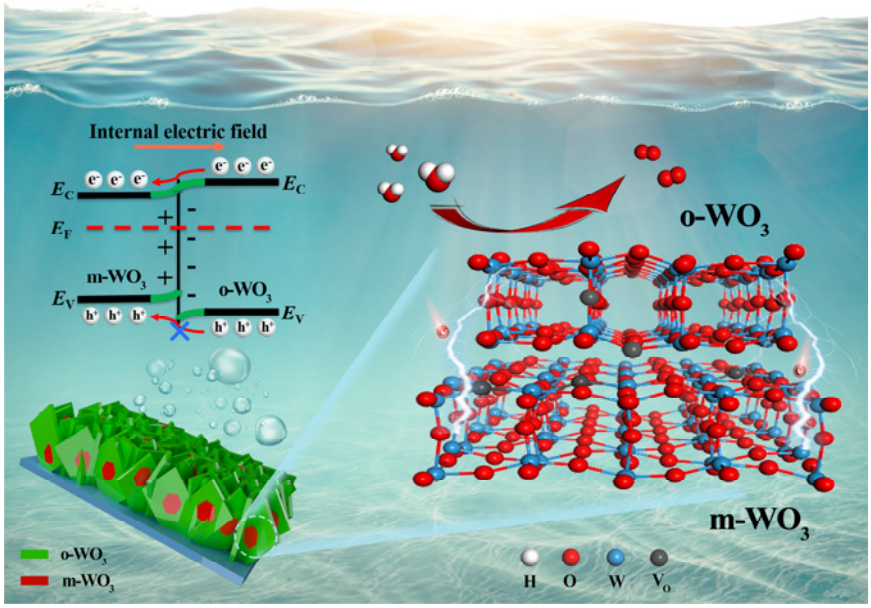

Fig. 9 Diagram of photoelectrocatalytic water splitting on o-WO_3/m-WO_3 phase junction.

based on the variable crystal phases of tungsten oxide. The formation of this phase interface effectively reduces the interface tension and defects caused by lattice mismatch, enhances the interface charge transfer, suppresses the charge recombination caused by defects as the recombination center, and realizes the low-defect and high-quality catalyst. Meanwhile, the o-WO_3/m-WO_3 phase junction with a crossed energy band arrangement structure realizes the rapid separation of photogenerated carriers and reduces the degree of electron–hole recombination. Furthermore, the oxygen vacancies, as surface active sites, effectively capture photogenerated electrons, improve the chemisorption ability of WO_3 towards water molecules, and promote the injection of photogenerated electrons into water molecules, thus increasing the activity of water splitting. The efficient separation and transfer of photocarriers are enhanced by the perfect phase junction interface and the well-matched staggered arrangement of energy band structures, thus significantly enhancing the redox capacity of the o-WO_3/m-WO_3 junction.

4 Conclusions

In summary, WO_3 system with monoclinic–orthorhombic phase junction is constructed by temperature-dependent phase transition through annealing treatment. The intimate phase junction interface and internal electric field modulate o-WO_3/m-WO_3 photoelectrode for boosting photoelectrocatalytic water splitting performance. The least lattice mismatch at the o-WO_3/m-WO_3 phase interface reduces the lattice distortion and promotes the formation of phase junctions. The o-WO_3/m-WO_3 phase junction with a staggered arrangement band structure dominates the charge transfer kinetics of photogenerated carrier separation, which is the fundamental reason for the improved hydrogen production activity. Meanwhile, oxygen vacancies act as a bridge connecting the phase junction for water splitting reaction, facilitating the transfer of electrons to water molecule. The o-WO_3/m-WO_3 phase junction demonstrates oxygen production rate of 7.93 μmol·cm^{-2}·h^{-1} under visible light irradiation, approximately four times that of pristine WO_3. High catalytic activity and structural stability were maintained after five cycle tests. This work presents a facile synthesis strategy for the construction o-WO_3/m-WO_3 phase junctions, and provides new insights into the rational design of phase junctions and the improvement of the intrinsic activity of semiconductor catalysts.

Acknowledgements

The financial support is gratefully acknowledged from the National Natural Science Foundation of China (Grant Nos. 62004137, 21878257, and 21978196), Natural Science Foundation of Shanxi Province (Grant No. 20210302123102), Key Research and Development Program of Shanxi Province (Grant No. 201803D421079), Scientific and

Technological Innovation Programs of Higher Education Institutions in Shanxi (Grant No. 2019L0156), Shanxi-Zheda Institute of Advanced Materials and Chemical Engineering (Grant No. 2022SX-TD002), Shanxi Provincial Key Innovative Research Team in Science and Technology (Grant No. 201605D13104510), and Research Project Supported by Shanxi Scholarship Council of China (Grant No. 2020-050).

Declaration of competing interest

The authors have no competing interests to declare that are relevant to the content of this article.

Electronic Supplementary Material

Supplementary material is available in the online version of this article at https://doi.org/10.1007/s40145-022-0653-8.

References

[1] Wang HL, Zhang LS, Chen ZG, *et al*. Semiconductor heterojunction photocatalysts: Design, construction, and photocatalytic performances. *Chem Soc Rev* 2014, **43**: 5234–5244.

[2] Kärkäs MD, Verho O, Johnston EV, *et al*. Artificial photosynthesis: Molecular systems for catalytic water oxidation. *Chem Rev* 2014, **114**: 11863–12001.

[3] Liu XQ, Iocozzia J, Wang Y, *et al*. Noble metal–metal oxide nanohybrids with tailored nanostructures for efficient solar energy conversion, photocatalysis and environmental remediation. *Energy Environ Sci* 2017, **10**: 402–434.

[4] Zhang GH, Zhang XQ, Meng Y, *et al*. Layered double hydroxides-based photocatalysts and visible-light driven photodegradation of organic pollutants: A review. *Chem Eng J* 2020, **392**: 123684.

[5] Hisatomi T, Kubota J, Domen K. Recent advances in semiconductors for photocatalytic and photoelectrochemical water splitting. *Chem Soc Rev* 2014, **43**: 7520–7535.

[6] Fujishima A, Honda K. Electrochemical photolysis of water at a semiconductor electrode. *Nature* 1972, **238**: 37–38.

[7] Dong ZB, Ding DY, Li T, *et al*. Ni-doped TiO_2 nanotubes photoanode for enhanced photoelectrochemical water splitting. *Appl Surf Sci* 2018, **443**: 321–328.

[8] Wang ZL, Mao X, Chen P, *et al*. Understanding the roles of oxygen vacancies in hematite-based photoelectrochemical processes. *Angew Chem Int Ed* 2019, **58**: 1030–1034.

[9] Lukatskaya MR, Kota S, Lin ZF, *et al*. Ultra-high-rate pseudocapacitive energy storage in two-dimensional transition metal carbides. *Nat Energy* 2017, **2**: 17105.

[10] Zhang J, Wang T, Liu P, *et al*. Engineering water dissociation sites in MoS_2 nanosheets for accelerated electrocatalytic hydrogen production. *Energy Environ Sci* 2016, **9**: 2789–2793.

[11] Sun M, Gao RT, He JL, *et al*. Photo-driven oxygen vacancies extends charge carrier lifetime for efficient solar water splitting. *Angew Chem Int Ed* 2021, **60**: 17601–17607.

[12] Liu XF, Zhou H, Pei SZ, *et al*. Oxygen-deficient WO_{3-x} nanoplate array film photoanode for efficient photoelectrocatalytic water decontamination. *Chem Eng J* 2020, **381**: 122740.

[13] Tahir M, Tasleem S, Tahir B. Recent development in band engineering of binary semiconductor materials for solar driven photocatalytic hydrogen production. *Int J Hydrogen Energ* 2020, **45**: 15985–16038.

[14] Gao JQ, Xue JB, Jia SF, *et al*. Self-doping surface oxygen vacancy-induced lattice strains for enhancing visible light-driven photocatalytic H_2 evolution over black TiO_2. *ACS Appl Mater Interfaces* 2021, **13**: 18758–18771.

[15] Gao JQ, Xue JB, Shen QQ, *et al*. A promoted photocatalysis system trade-off between thermodynamic and kinetic via hierarchical distribution dual-defects for efficient H_2 evolution. *Chem Eng J* 2022, **431**: 133281.

[16] Zhang J, Xu Q, Feng ZC, *et al*. Importance of the relationship between surface phases and photocatalytic activity of TiO_2. *Angew Chem Int Ed* 2008, **47**: 1766–1769.

[17] Wang X, Xu Q, Li MR, *et al*. Back cover: Photocatalytic overall water splitting promoted by an α–β phase junction on Ga_2O_3 (Angew. Chem. Int. Ed. 52/2012). *Angew Chem Int Ed* 2012, **51**: 13180.

[18] Shen QQ, Xue JB, Li Y, *et al*. Construction of CdSe polymorphic junctions with coherent interface for enhanced photoelectrocatalytic hydrogen generation. *Appl Catal B Environ* 2021, **282**: 119552.

[19] Fu Q, Wang XJ, Han JC, *et al*. Phase-junction electrocatalysts towards enhanced hydrogen evolution reaction in alkaline media. *Angew Chem Int Ed* 2021, **60**: 259–267.

[20] Liu FL, Shi R, Wang Z, *et al*. Direct Z-scheme hetero-phase junction of black/red phosphorus for photocatalytic water splitting. *Angew Chem Int Ed* 2019, **58**: 11791–11795.

[21] Zhao Y, Balasubramanyam S, Sinha R, *et al*. Tuning structural properties of WO_3 thin films for photoelectrocatalytic water oxidation. *ACS Appl Energy Mater* 2018, **1**: 5887–5895.

[22] Tian W, Chen C, Meng LX, *et al*. PVP treatment induced gradient oxygen doping in In_2S_3 nanosheet to boost solar water oxidation of WO_3 nanoarray photoanode. *Adv Energy Mater* 2020, **10**: 1903951.

[23] Tatsuma T, Saitoh S, Ohko Y, *et al*. TiO_2–WO_3 photoelectrochemical anticorrosion system with an energy storage ability. *Chem Mater* 2001, **13**: 2838–2842.

[24] Sadeghzadeh-Attar A. Photocatalytic degradation evaluation of N–Fe codoped aligned TiO_2 nanorods based on the effect of annealing temperature. *J Adv Ceram* 2020, **9**: 107–122.

[25] Zheng HD, Ou JZ, Strano MS, *et al*. Nanostructured tungsten oxide—Properties, synthesis, and applications. *Adv Funct Mater* 2011, **21**: 2175–2196.

[26] Zhan FQ, Liu Y, Wang KK, *et al*. Oxygen-deficient nanofiber WO_{3-x}/WO_3 homojunction photoanodes synthesized via a novel metal self-reducing method. *ACS Appl Mater Interfaces* 2019, **11**: 39951–39960.

[27] Wang N, Zhu J, Zheng XJ, *et al*. A facile two-step method for fabrication of plate-like WO_3 photoanode under mild conditions. *Faraday Discuss* 2014, **176**: 185–197.

[28] Wang JC, Zhou TS, Zhang Y, *et al*. The design of high performance photoanode of CQDs/TiO_2/WO_3 based on DFT alignment of lattice parameter and energy band, and charge distribution. *J Colloid Interf Sci* 2021, **600**: 828–837.

[29] Idris MS, Osman RAM. Structure refinement strategy of Li-based complex oxides using GSAS–EXPGUI software package. *Adv Mater Res* 2013, **795**: 479–482.

[30] Yan JQ, Wang T, Wu GJ, *et al*. Tungsten oxide single crystal nanosheets for enhanced multichannel solar light harvesting. *Adv Mater* 2015, **27**: 1580–1586.

[31] Zeng QY, Li JH, Bai J, *et al*. Preparation of vertically aligned WO_3 nanoplate array films based on peroxotungstate reduction reaction and their excellent photoelectrocatalytic performance. *Appl Catal B Environ* 2017, **202**: 388–396.

[32] Zhang XH, Lu XH, Shen YQ, *et al*. Three-dimensional WO_3 nanostructures on carbon paper: Photoelectrochemical property and visible light driven photocatalysis. *Chem Commun* 2011, **47**: 5804–5806.

[33] Li YT, Liu ZF, Li JW, *et al*. An effective strategy of constructing a multi-junction structure by integrating a heterojunction and a homojunction to promote the charge separation and transfer efficiency of WO_3. *J Mater Chem A* 2020, **8**: 6256–6267.

[34] Zhao FF, Sheng HX, Sun QP, *et al*. Harvesting the infrared part of solar light to promote charge transfer in Bi_2S_3/WO_3 photoanode for enhanced photoelectrochemical water splitting. *J Colloid Interf Sci* 2022, **621**: 267–274.

[35] Tian H, Cui XZ, Zeng LM, *et al*. Oxygen vacancy-assisted hydrogen evolution reaction of the Pt/WO_3 electrocatalyst. *J Mater Chem A* 2019, **7**: 6285–6293.

[36] Wei Z, Wang WC, Li WL, *et al*. Steering electron–hole migration pathways using oxygen vacancies in tungsten oxides to enhance their photocatalytic oxygen evolution performance. *Angew Chem Int Ed* 2021, **60**: 8236–8242.

[37] Owens-Baird B, Xu JY, Petrovykh DY, *et al*. NiP_2: A story of two divergent polymorphic multifunctional materials. *Chem Mater* 2019, **31**: 3407–3418.

[38] Niu MT, Huang F, Cui LF, *et al*. Hydrothermal synthesis, structural characteristics, and enhanced photocatalysis of SnO_2/α-Fe_2O_3 semiconductor nanoheterostructures. *ACS Nano* 2010, **4**: 681–688.

[39] Liu JF, Wang FF, Chen XB, *et al*. Unraveling the lattice matching effect in surface phase junctions for interfacial charge separation. *J Phys Chem C* 2021, **125**: 14188–14194.

[40] Zhou WW, Cheng CW, Liu JP, *et al*. Epitaxial growth of branched α-Fe_2O_3/SnO_2 nano-heterostructures with improved lithium-ion battery performance. *Adv Funct Mater* 2011, **21**: 2439–2445.

[41] Song JJ, Huang ZF, Pan L, *et al*. Oxygen-deficient tungsten oxide as versatile and efficient hydrogenation catalyst. *ACS Catal* 2015, **5**: 6594–6599.

[42] Yang WY, Chen Y, Gao S, *et al*. Post-illumination activity of Bi_2WO_6 in the dark from the photocatalytic "memory" effect. *J Adv Ceram* 2021, **10**: 355–367.

[43] Gao JQ, Shen QQ, Guan RF, *et al*. Oxygen vacancy self-doped black TiO_2 nanotube arrays by aluminothermic reduction for photocatalytic CO_2 reduction under visible light illumination. *J CO_2 Util* 2020, **35**: 205–215.

[44] Wu J, Li LY, Li XA, *et al*. A novel 2D graphene oxide modified α-$AgVO_3$ nanorods: Design, fabrication, and enhanced visible-light photocatalytic performance. *J Adv Ceram* 2022, **11**: 308–320.

[45] Fan LL, Lei SL, Kheimeh Sari HM, *et al*. Controllable S-vacancies of monolayered Mo–S nanocrystals for highly harvesting lithium storage. *Nano Energy* 2020, **78**: 105235.

[46] Corby S, Francàs L, Kafizas A, *et al*. Determining the role of oxygen vacancies in the photoelectrocatalytic performance of WO_3 for water oxidation. *Chem Sci* 2020, **11**: 2907–2914.

[47] Yang YR, Chen JM, Liu XL, *et al*. Oxygen vacancy-mediated WO_3 nanosheets by etched {200} facets and the efficient visible-light photocatalytic oxygen evolution. *New J Chem* 2019, **43**: 16391–16395.

[48] Sotelo-Vazquez C, Quesada-Cabrera R, Ling M, *et al*. Evidence and effect of photogenerated charge transfer for enhanced photocatalysis in WO_3/TiO_2 heterojunction films: A computational and experimental study. *Adv Funct Mater* 2017, **27**: 1605413.

[49] Liu JJ. Origin of high photocatalytic efficiency in monolayer g-C_3N_4/CdS heterostructure: A hybrid DFT study. *J Phys Chem C* 2015, **119**: 28417–28423.

[50] Jiang LS, Li J, Li Y, *et al*. Promoted charge separation from nickel intervening in $[Bi_2O_2]^{2+}$ layers of Bi_2O_2S crystals for enhanced photocatalytic CO_2 conversion. *Appl Catal B Environ* 2021, **294**: 120249.

[51] Li Y, Mei Q, Liu ZJ, *et al*. Fluorine-doped iron oxyhydroxide cocatalyst: Promotion on the WO_3 photoanode conducted photoelectrochemical water splitting. *Appl Catal B Environ* 2022, **304**: 120995.

[52] Peng JJ, Shen J, Yu XH, *et al*. Construction of LSPR-enhanced 0D/2D CdS/MoO_{3-x} S-scheme heterojunctions for visible-light-driven photocatalytic H_2 evolution. *Chinese J Catal* 2021, **42**: 87–96.

[53] Li Y, Xue JB, Shen QQ, *et al*. Construction of a ternary spatial junction in yolk–shell nanoreactor for efficient photo-thermal catalytic hydrogen generation. *Chem Eng J* 2021, **423**: 130188.

[54] Zhang GH, Yuan XX, Xie B, *et al*. S vacancies act as a bridge to promote electron injection from Z-scheme

heterojunction to nitrogen molecule for photocatalytic ammonia synthesis. *Chem Eng J* 2022, **433**: 133670.

[55] Jin PX, Wang L, Ma XL, *et al*. Construction of hierarchical $ZnIn_2S_4$@PCN-224 heterojunction for boosting photocatalytic performance in hydrogen production and degradation of tetracycline hydrochloride. *Appl Catal B Environ* 2021, **284**: 119762.

[56] Li Y, Wang QZ, Hu XS, *et al*. Constructing NiFe-metal–organic frameworks from NiFe-layered double hydroxide as a highly efficient cocatalyst for $BiVO_4$ photoanode PEC water splitting. *Chem Eng J* 2022, **433**: 133592.

[57] Li YT, Liu ZF, Guo ZG, *et al*. Efficient WO_3 photoanode modified by Pt layer and plasmonic Ag for enhanced charge separation and transfer to promote photoelectrochemical performances. *ACS Sustain Chem Eng* 2019, **7**: 12582–12590.